Carbon Emissions are Underpriced Due to the Snow Albedo Feedback Effect*

Sofia P. Baker† J. Isaac Miller†

Abstract

To balance the tradeoff between economic activity and climate goals by internalizing the cost of emissions, integrated assessment models calculate a social cost of carbon. Embedded in such models are physical energy balance climate models that typically employ temporally constant climate parameters. We examine the empirical effects of changing surface albedo over time. To this end, we leverage satellite data since 2001 in a state-space model in conjunction with an adaptation of the reverse Kalman filter to estimate incoming energy less albedo over 1850-2023. The results show a decreasing albedo trend over most of the sample. Our estimates are consistent with the snow albedo feedback (SAF) where melting ice leads to declines in albedo, thereby causing increased heat absorption at the surface and further melting. Together, these findings indicate that the heating effects of carbon emissions are amplified by the SAF, the omission of which in the carbon pricing decision leads to underpricing.

This Version: September 30, 2026

JEL Classification: C32, Q54

Key words and phrases: climate change, energy balance climate model, snow albedo effect, carbon pricing

*This research draws heavily on a forthcoming dissertation chapter by the first author under the supervision of the second author. Both authors contributed to all aspects of this manuscript. The authors are grateful to Buz Brock for constructive comments. The usual caveat applies.

†Department of Economics, University of Missouri

1 Introduction

Because hydrocarbons are the main driver of energy generation, most economic activity emits some amount of carbon (Alajingi and Marimuthu, 2023). Common responses to the externality caused by carbon emissions, carbon taxes or tradable pollution permits, require internalizing the externality by way of a price of carbon emissions (Jenkins, 2014), placing carbon pricing at the center of contemporary climate and economic policy discussions (Baranzini et al., 2017).

Integrated Assessment Models (IAMs) are commonly used to balance climate and economic growth goals. IAMs incorporate future carbon emissions projections in response to climate policies and incorporate interactions between climate, social, and economic factors to evaluate social costs of carbon emissions (Weyant, 2017). The most well-known IAMs[1] utilize a constant climate sensitivity parameter (Calel and Stainforth, 2017) in an embedded energy balance climate model (EBCM) to estimate the rise in global mean temperature in response to an increase – often a doubling – of CO_2 in the atmosphere. Such estimates then feed into pricing carbon emissions.

However, a constant climate sensitivity parameter cannot capture changes to albedo, specifically surface albedo, the fraction of incoming energy from the sun that reaches the surface of the Earth and is reflected. Albedo is important in the climate literature because changes in albedo have been theorized to amplify climate change through a positive feedback loop between temperature and frozen surfaces, referred to as the SAF. Specifically, as the planet heats up, ice melts, which exposes less reflective surfaces and leads to increased heat absorption at the surface, which then leads to subsequent melting and heating.

Because carbon emissions contribute to global temperature increases, the SAF could amplify the heating effects of these emissions. Based on temperature, anthropogenic and natural forcings, and snow cover, Kaufmann and Pretis (2023) find that the direct effect of carbon emissions on temperature is amplified by 3.4% over 1972-2008 due to the SAF. Their work on the SAF motivates further research into estimating albedo directly. Although early albedo measurements exist, regular and reliable albedo estimates rely on satellite measurements. The availability of satellites naturally limits the span of such measurements rendering them difficult to incorporate in long-term studies of the forcing-temperature relationship.

We propose a statistical state-space representation of a physical EBCM model to analyze how the SAF and changes in planetary albedo more generally amplify the effects of carbon emissions on temperature, and hence how changes in albedo may affect pricing those emissions. We adapt the reverse Kalman filter (RKF) (Fraser and Potter, 1969; Taplin, 1998) to an environment with a series that is latent only prior to 2001, and we propose a maximum likelihood procedure for estimating

[1] Dynamic Integrated model of Climate and the Economy (DICE), the Climate Framework for Uncertainty, Negotiation and Distribution (FUND), and the Policy Analysis for the Greenhouse Effect (PAGE).

the model parameters. By implementing the RKF with satellite albedo estimates starting in 2001, we back out estimates of albedo from the pre-satellite era. To the best of the authors' knowledge, this is the first study to estimate a historical time series of global albedo.[2]

We find that surface albedo has declined over time in a manner consistent with SAF theory. For example, albedo changes from 1943-2023 account for a 1.5 W m^{-2} increase in the Earth surface energy budget, more than 90% of the direct effect of carbon emissions over that time (1.6 W m^{-2}). Such a large magnitude strongly suggests that ignoring the SAF by assuming constant climate sensitivity risks substantially underpricing carbon emissions.

The rest of this paper is structured as follows. Because our core focus lies in a new methodology and new estimates of albedo, Section 2 provides a detailed discussion of the literature on measuring albedo. Readers well versed in this literature may safely skip this section without losing context for the remainder of the paper. We discuss the data and methods respectively that we utilize in estimating albedo in Sections 3 and 4 respectively. We present our empirical results and albedo estimates in Section 5 with discussions on the effects of various drivers of albedo changes and implications of those changes for carbon pricing. Section 6 concludes.

2 A Detailed Review of Albedo

The term "albedo" was first coined by Swiss mathematician Johann Heinrich Lambert referring to the fraction of light radiated back from a surface in optics (Mach, 2013; Perkins, 2020). American astronomer George P. Bond first used the term in reference to the reflectiveness of planets (Bond, 1861). Specifically, planetary albedo is the fraction of incoming solar energy reflected by the Earth back to space. Bond postulated that surface and atmospheric factors shape the reflection of astronomical objects, and these factors form the basis for measuring planetary albedo to this day.

2.1 Planetary/Top-of-Atmosphere (TOA) and Surface Albedo Measurement

Planetary albedo is derived from the direct relationship between the outgoing flux at the top of the atmosphere (TOA) and the incoming solar flux at the top of the atmosphere (Stephens et al., 2015), and the terms TOA albedo and planetary albedo are used interchangeably in the literature (Stephens et al., 2015; Liang et al., 2019; Zhan and Liang, 2022; Nikolov and Zeller, 2024). Modern albedo estimates rely on satellite systems dedicated to the analysis of the Earth's radiation budget, such as the Earth Radiation Budget Experiment (ERBE) and the Clouds and the Earth's Radiant Energy System (CERES) and are restricted to the satellite era as a result. CERES[3] provides

[2]Song et al. (2021) combine current satellite observations with surface albedo look-up maps and reanalysis data to extract surface albedo dating back to 850 AD in China.

[3]https://ceres.larc.nasa.gov/data/

incoming flux and outgoing flux measurements dating back to March 2000. These are considered the most accurate measurements of TOA fluxes (Zhan et al., 2019), and is therefore one of the most widely used sources of data on TOA albedo (by Stephens et al. (2015), Hansen et al. (2025), *inter alia*). However, the longest series of albedo estimates using satellites extends back to 1979.[4]

Before the use of satellites, TOA albedo was primarily measured using so-called earthshine methods which infer the reflectiveness of the Earth based on the observed brightness of the moon. Early studies using this method published in 1913, 1928 and 1933 calculate TOA albedo estimates of 89%, 29% and 39% respectively (Stephens et al., 2015), with such large variations in estimates over a short period of time indicating much lower precision compared to modern estimates. The technology to collect the data needed to calculate albedo using earthshine methods has improved over time (Wu et al., 2023) bringing into question the earliest earthshine estimates of Very (1913) and Danjon (1928, 1933). Even if we accept the inaccuracies of the early calculations, they were collected and calculated only sporadically (Goode et al., 2001; Stephens et al., 2015; Goode et al., 2021), hindering our ability to generate time series for long-term climate and economic analysis.

Alternative methods for calculating TOA albedo rely on radiation budget calculations with assumptions about cloud cover and surface characteristics, again with estimates varying extensively (Stephens et al., 2015). In a pioneering study, Abbott and Fowle (1908) estimate planetary albedo by separating the planet into subsections by type of cloud cover and computing radiation movements. Subsequent researchers use similar climate modeling to estimate planetary albedo and leverage improved climate parameter estimates due to advances in data collection technology and sampling frequency (Fritz, 1949; Houghton, 1954).

Satellite technology has enabled researchers to study changes in albedo across time with improved precision. For instance, Kato (2009) uses satellite data from 2000-2004 to show global mean TOA albedo exhibits only small changes between years. Likewise, Stephens et al. (2015) survey the literature on global TOA albedo and find that estimates of TOA albedo have not changed much since the advent of satellites in 1959. More recently, Goode et al. (2021) find a decline in albedo. Specifically, the earthshine estimates of TOA albedo made by those authors decline from 1998-2017 and correspond to a forcing of approximately 0.5 watts per square meter (W m^{-2}), while the CERES data from 2001-2017 show a TOA albedo decrease corresponding to a forcing of 0.7 W m^{-2}. Both Goode et al. (2021) and Hansen et al. (2025) note a sharp decline in the CERES data starting in 2015 which is clearly beyond the last year considered by Stephens et al. (2015). Nikolov and Zeller (2024) claim that global warming can largely be explained by large decreases in TOA albedo documented over this time frame.

[4]The CM SAF Cloud, Albedo and surface Radiation (CLARA) data set provides albedo estimates from 1979-2020 (Riihelä et al., 2024) primarily based on narrowband AVHRR (Advanced Very High Resolution Radiometer) measurements.

Analogous to TOA albedo, surface albedo is the percentage of incoming solar radiation that reaches the surface of the Earth and is reflected (Riihelä et al., 2024), thereby serving as a contributor to planetary albedo along with atmospheric scattering (Stephens et al., 2015). Several algorithms have been used to calculate surface albedo from TOA albedo. For instance, Li and Garand (1994) estimate surface albedo from ERBE TOA albedo using a formula depending on solar zenith angle and total precipitable water which they show to be robust across several surface types. Similarly, He et al. (2014) compare observations from nine satellite-based surface albedo data sets that convert satellite observations to surface albedo estimates using multiple algorithms for removing the effects of atmosphere and cloud cover.

The earliest earthshine observations by Very (1913) and Danjon (1928, 1933) focused on obtaining TOA albedo measurements (Hunt et al., 1986) and at best could only give information on surface albedo based on assumptions of atmospheric and cloud conditions at the time the estimates were made. Mengyao et al. (2023) examine nine different land surface albedo data sets over various time spans (some starting circa 1980 and others circa 2000) and found no long-term trend in land surface albedo. However, Mengyao et al. (2023), Riihelä et al. (2024) and Qu et al. (2015) note that commonly available surface albedo datasets have difficulty estimating the albedo of ocean surfaces, sea ice and ice over polar regions, all of which are important sources of albedo and hence important in studying the SAF (Previdi et al., 2021; Kaufmann and Pretis, 2023).

2.2 Drivers of Change in Albedo

What causes albedo to change over time? Given that ice is among the most reflective surfaces on Earth, an obvious driver is the extent of ice on the planet. Using a simple statistical model, Diebold and Rudebusch (2022) find that the Arctic sea ice extent has decreased at an accelerated rate in recent years. Specifically, they project a 60% probability of a September ice-free Arctic appearing sometime in the 2030s, a much more concerning projection than that made by CMIP5 models. Similarly, Diebold and Rudebusch (2023) emphasize the importance of accurately modeling receding ice lines by showing that Global Climate Models tend to underestimate the effect of carbon emissions on Arctic sea ice extent.

Another set of drivers of albedo change is dark materials such as black carbon (Forster et al., 2024) or algae (Williamson et al., 2020) that increasingly cover snow and ice. For example, Kang et al. (2020) find that black carbon accumulation is responsible for about 20% of the drop in albedo in the Tibetan plateau region. Decreases in surface albedo from black carbon on snow are also supported by a laboratory experiment conducted by Hadley and Kirchstetter (2012) comparing the albedo of snow with and without black carbon accumulation, the results of which are consistent with both model and field-based estimates. Biological organisms can also cause similar decreases in albedo. Field sampling conducted by Williamson et al. (2020) provides evidence that algae blooms

increase heat absorption of the Greenland ice sheet and account for a large fraction of albedo variability in the region. Chavez et al. (2026) develop a model in which change in albedo due to glacial microalgae is large enough to tip the ecosystem into a stable "hothouse" state.

Changes to land use through actions such as deforestation and construction of human habitats form a significant anthropogenic contributor to surface albedo changes in recent history. Deforestation has been shown to increase albedo given that forests are dark and hence absorb light (Mylne and Rowntree, 1992; Santos Orozco et al., 2023). Urbanization has been shown both to decrease (Tang et al., 2018) and to increase (Hu et al., 2016) albedo depending on type of surface change. Ouyang et al. (2022) analyze the global warming effect of urbanization and find a planetary heating effect that is projected to continue. To counter this effect, some building projects have specifically aimed to deter heat absorption and have been shown to successfully reduce global warming effects (Cotana et al., 2014) by increasing albedo.

Natural climate cycles are another driver of surface albedo variability. For example, Wyatt and Curry (2014) study the role of the Eurasian Arctic shelf sea ice in explaining the previously-identified stadium wave pattern which appears to cycle around the northern hemisphere every ∼50-80 years as indicated through the coordination of a variety of climate indices. Wyatt and Curry (2014) identify variations in the formation of sea ice in the Eurasian Arctic ice shelf as a significant physical mechanism behind the stadium wave, with increased ice formation corresponding to cooling phases of the cycle. This finding suggests the stadium wave pattern may be correlated with surface albedo given the large difference in ocean and sea ice albedoes. Similarly, the Atlantic Multidecadal Oscillation is characterized by warm and cool periods in surface temperature (Knight et al., 2006) and could therefore affect albedo due to ice formation, as could changes in the ocean's heat uptake (Kosaka and Xie, 2013).

Finally, changes in albedo itself drive changes in albedo by way of the SAF. Budyko (1969) and Held and Suarez (1974) provide a theoretical basis for the SAF and that explains the formation of ice ages and a hypothetical frozen state so-called "snowball Earth." The SAF has since been studied widely (Déry and Brown, 2007; Qu and Hall, 2007, 2014; Thackeray and Fletcher, 2016). Kaufmann and Pretis (2023) refute previous larger estimates of the SAF with an error correction model incorporating temperature, forcing, and snow cover data. The SAF estimate from Kaufmann and Pretis (2023) of 3.4% amplification is approximately an order of magnitude smaller than estimates obtained through more complex process-based climate models. The latter authors attribute the discrepancy to an oversensitivity of snow cover to temperature increases in process-based models.

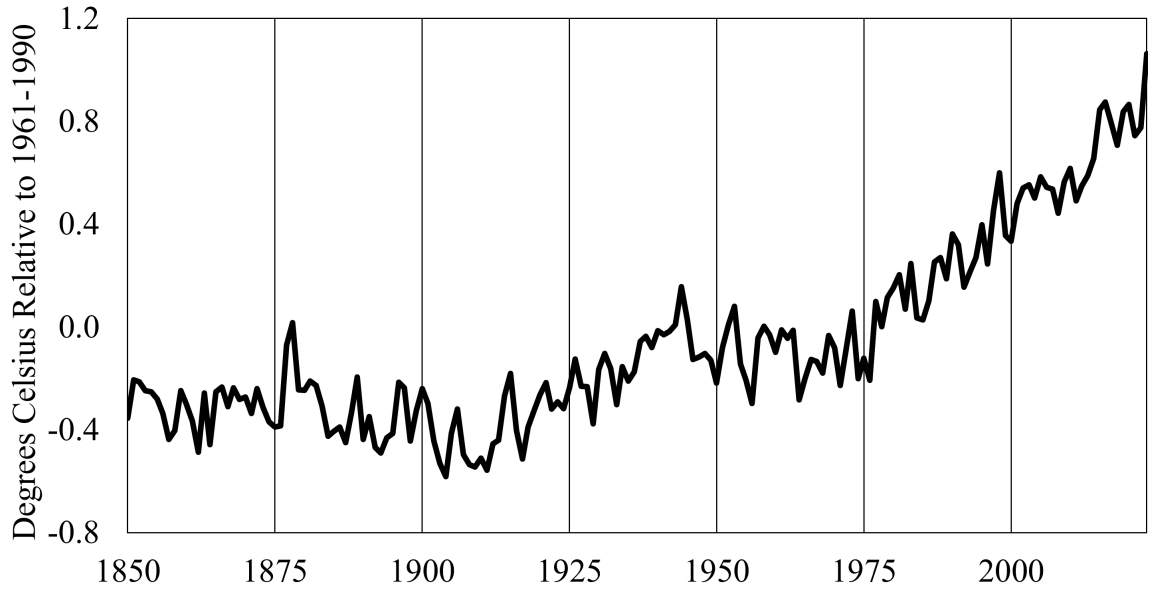


Figure 1: Global average annual temperature anomalies in degrees Celsius relative to the 1961-1990 base period from HadCRUT5.

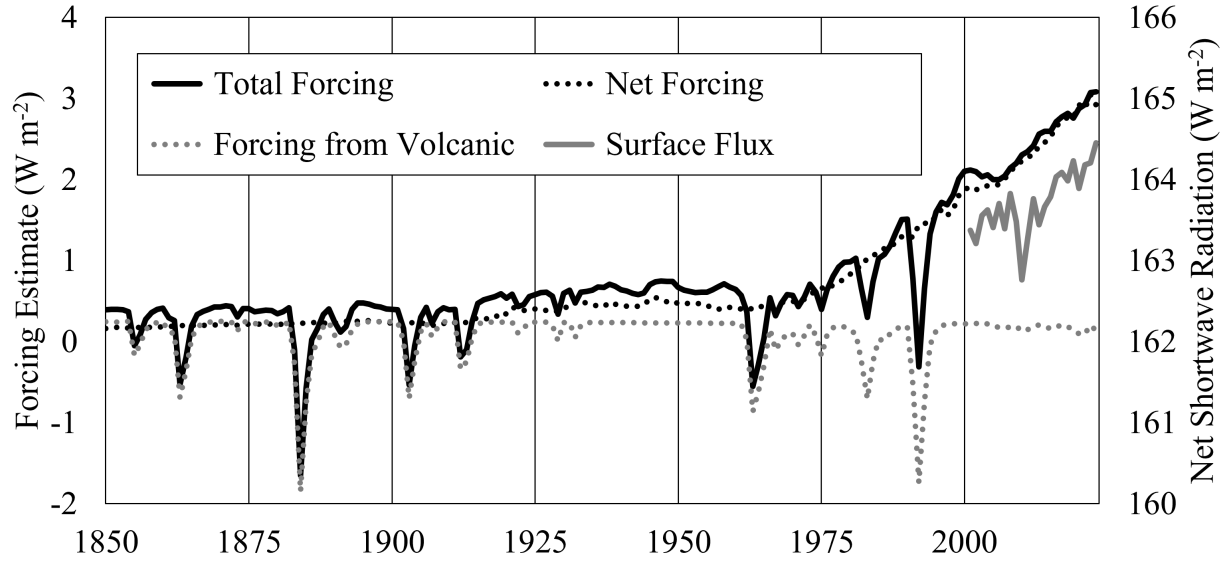


Figure 2: Forcing series from Forster et al. (2024) over 1850-2023 shows the effect of each forcing category on the top-of-atmosphere energy balance relative to 1750. Total forcing includes solar, volcanic, and anthropogenic forcing. Net forcing excludes solar, volcanic, and changes in albedo from black carbon on snow and land use. An annualized surface flux series from CERES is shown over 2001-2023.

3 Data

3.1 Temperature Anomalies and Climate Forcings

Figure 1 shows the temperature anomaly data used in our analysis. Specifically, we use the HadCRUT5.0.2.0 non-infilled annual global average data series.[5] The HadCRUT5 data set combines data from the HadSST sea-surface and CRUTEM land surface temperature data sets. To generate temperature anomalies (in Kelvin or degrees Celsius), the HadCRUT5 data set establishes a base period and displays a deviation from the base period average for each year. Specifically, HadCRUT5 uses 1961-1990 as the base period due to the best sample coverage occurring during this time.

Temperature measurement methods have evolved significantly over time. Prior to WWII, sea-surface temperatures were largely collected by taking the temperature of sea water extracted using uninsulated buckets from the ocean (Folland and Parker, 1995). After WWII, temperature collection transitioned to more reliable methods including collection methods built directly into the ship (i.e., engine inlets), insulated buckets (Folland and Parker, 1995) and more recently, the use of buoys (Kennedy et al., 2011). The widespread use of uninsulated buckets in sea-surface temperature collection prior to 1940 biased temperatures downward because heat escaped from the water (Folland and Parker, 1995) and for this reason the HadSST team conduct bias corrections based on estimated shares of different collection types combined with physical models of heat transfer from the buckets. The HadSST data set is reported as a 200-member ensemble by varying the unknown bias correction parameters within reasonable ranges (Kennedy et al., 2019). Regarding uncertainties in the CRUTEM data, the primary change in land surface temperature measurements has been an increase in station coverage across time (Jones and Moberg, 2003) which has also occurred for sea-surface temperatures (Kennedy et al., 2011). As with HadSST, the HadCRUT5 data set reports a 200-member ensemble to account for systematic bias in measurements, as well as the series of ensemble mean temperature anomalies used in this study.

Figure 2 shows the forcing series used in our analysis. We use effective radiative forcing (or simply forcing) data generated by Forster et al. (2024)[6] which includes multiple types of anthropogenic forcing and natural forcing from solar and volcanic events. Forcing data are provided in W m^{-2} and can be interpreted as the effect of a forcer on the energy balance at the top of the atmosphere, where positive values indicate energy added to the system. Forcings from Forster et al. (2024) update forcings from Ch 7 of AR6 WGI. Radiative forcings are adjusted to include additional downstream effects that are independent of surface temperature effects to maintain separation from climate feedbacks such as the SAF. The Intergovernmental Panel on Climate Change shifted to the use of

[5] Downloaded on 2025-04-19 from https://crudata.uea.ac.uk/cru/data/temperature/ (HadCRUT version 5.0.2.0 "GL" series)

[6] Data version v2024.05.29b downloaded on 2025-04-19 from https://zenodo.org/records/11388387

ERF as its primary forcing measure in AR5 because it includes broader effects of radiative forcings and continued its use in AR6 (Forster et al., 2021).

3.2 Surface Flux

We use CERES-EBAF edition 4.2.1 monthly global mean computed surface fluxes, or simply flux.[7] CERES data are available monthly from March 2000. Energy from the sun reaches the surface in the form of shortwave radiation (Trenberth et al., 2009) and reflected solar radiation remains in shortwave form. Net shortwave flux at the surface is given by subtracting upward (outgoing) shortwave radiation from downward (incoming) shortwave radiation, seasonally adjusted versions of which are illustrated in Figure 3. We aggregate the difference between the two series (without seasonal adjustment) to an annual level using data from 2001 to 2023, which is the flux series shown in Figure 2 alongside the series of forcings and is that used in our analysis.

Albedo is calculated as the ratio of upward to downward shortwave radiation (Stephens et al., 2015), and Figure 4 shows the ratio calculated using the annual averages of the two series. We use all-sky fluxes for this calculation, as opposed to clear-sky fluxes, which are computed fluxes for a scenario where clouds are omitted (Wild et al., 2019). Although clear-sky fluxes are useful for estimating the influence of clouds on the Earth energy budget (Wild et al., 2019), all-sky fluxes are closer to actual surface fluxes and are more accurate for estimating the SAF (Stephens et al., 2015).

CERES data are known to measure shortwave radiation with bias, especially around the poles (Kato et al., 2018), and albedo may be underestimated by 8% in April-September in the Arctic compared to estimates collected at surface sites (Huang et al., 2022). However, the spatial patterns of CERES-EBAF total surface irradiances fit with past studies (Loeb et al., 2022; Kato et al., 2025) and the time series of surface irradiances in CERES-EBAF are very close to time series of observations collected at surface sites (Kato et al., 2018) which means that while the using the CERES data underestimates albedo at the poles, it is more reliable on a global scale (Huang et al., 2022). Kato et al. (2018) report uncertainty in downward and upward shortwave radiation of 3 and 4 W m^{-2} respectively, which are not inconsequential in comparison with the decadal mean values of these series, 187.1 W m^{-2} and 23.1 W m^{-2} respectively. Fortunately, time-invariant bias and measurement error should not qualitatively affect trends detected in our results.

Kato et al. (2018) compare CERES-EBAF estimates of downward shortwave radiation at the surface to ocean and land surface observation sites and identify the driver of downward shortwave radiation variability as cloud and atmospheric factors. The downward radiation estimates shown in Figure 3, seasonally adjusted by regressing out monthly fixed effects, have notable minima in

[7] Downloaded on 2025-05-29 from https://ceres.larc.nasa.gov/data/

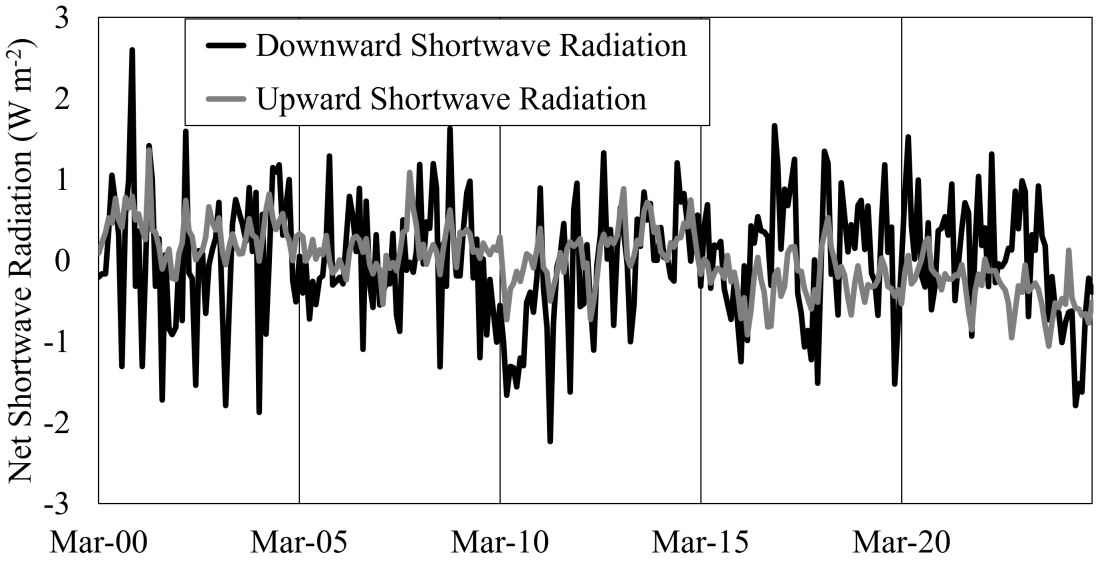


Figure 3: Seasonally adjusted downward and upward shortwave radiation at the surface data from CERES collected via satellite and climate calibration.

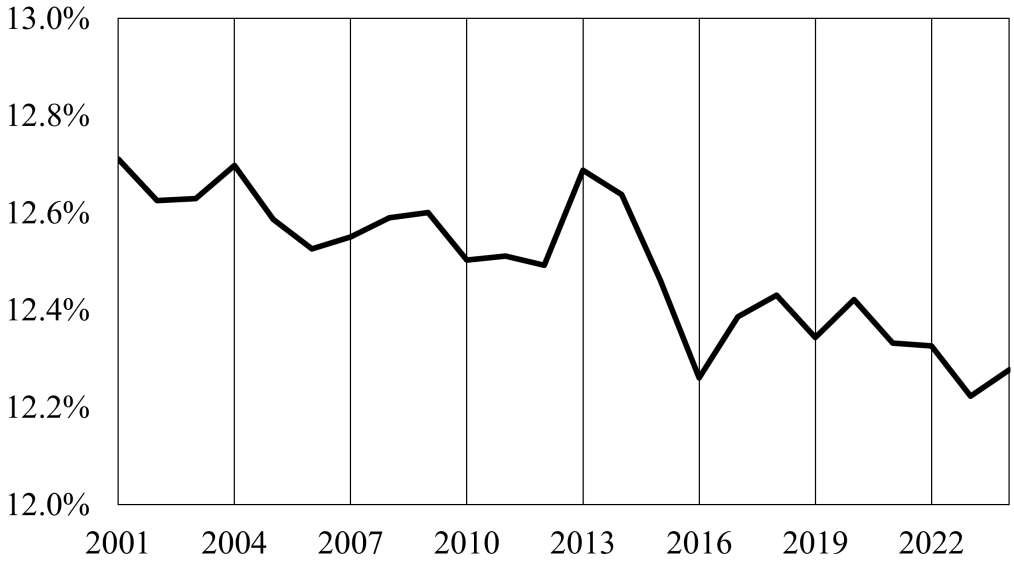


Figure 4: Surface albedo calculated from CERES data by dividing upward radiation by downward radiation.

2010 and again towards the end of the sample, but are otherwise relatively stable. In contrast, an evident decreasing trend in upward shortwave radiation suggests decreasing reflectiveness of the surface. Taken together, these trends suggest that the increase in the CERES net shortwave radiation shown in Figure 2 is largely explained by the more obvious decline in upward radiation (shown as seasonally adjusted in the figure) and hence by changes in albedo rather than cloud and atmospheric factors.

Revisiting Figure 4, we see a clearly decreasing trend in surface albedo roughly corresponding to the increasing net shortwave radiation trend in Figure 3. Moreover, it appears that the surface albedo decline has accelerated in recent years, which is consistent with acceleration of TOA albedo declines shown by Hansen et al. (2025) starting around 2015.

4 Methods

4.1 Zero-dimensional Energy Balance Climate Model

Our model is derived from the zero-dimensional benchmark EBCM used by Brock and Miller (2024) and inspired by those of Budyko (1969) and Sellers (1969), a simple model relating global temperature change to incoming energy to the planet, outgoing radiation, and forcing. Zero-dimensional means that heat transfer occurs only in and out of the atmosphere, but not horizontally by latitude. All else equal, when an EBCM is forced – i.e., an exogenous change in the energy system is imposed (Castle et al., 2024) – temperature has to change. Although very simple representations, EBCMs are commonly used to investigate specific aspects of the climate and are often used to study the effects of forcing on globally aggregated temperature. Given the simplicity of EBCMs, it is easier to extract macroscopic mechanisms which could broadly affect future research and policy decisions (North and Kim, 2017).

Our baseline EBCM is given by

$$C\partial_t T(t) = Q(t) - (A + BT(t)) + E(t) \tag{1}$$

or

$$\partial_t T(t) = \frac{1}{C}Q(t) - \frac{1}{C}(A + BT(t)) + \frac{1}{C}E(t) \tag{2}$$

where C is a heat capacity parameter, $T(t)$ and $E(t)$ are surface temperature and forcing at time t, $A + BT(t)$ is outgoing radiation and $Q(t)$ is incoming radiation net albedo at the Earth's surface – as opposed to the top of the atmosphere – at time t. In order to study albedo changes across time, we modify the zero-dimensional EBCM of Brock and Miller (2024) by converting a constant Q to $Q(t)$ which varies over time. Allowing albedo to vary over time is a flexible way of capturing

Table 1: Symbols, units and descriptions of the main quantities, variables, and parameters of the climate and econometric models from Brock and Miller (2024)

Symbol	**Unit**	**Description**
Energy Balance Model and Data		
$E(t), E_t^{*A}, E_t^{*V}$	W m^{-2} (Watts/square meter)	Total, non-volcanic, volcanic forcing (anomaly)
$T(t), T_t^*$	K (Kelvin)	Surface temperature (anomaly)
$\partial_t T(t)$, ΔT_{t+1}^*	K ∇^{-1} (Kelvin per time increment)	Surface temperature increase
$Q(t), Q_t^*$	W m^{-2}	Incoming radiation less albedo (anomaly)
$C > 0$	W m^{-2} K^{-1} ∇	Heat capacity
$A > 0$	W m^{-2}	Intercept parameter (removed in estimation)
$B > 0$	W m^{-2} K^{-1}	Sensitivity of outgoing long-wave radiation
State-Space Model Parameters		
β_0	W m^{-2}	Intercept
β_1	∇^{-1}	Coefficient on surface temperature anomaly
β_2	W^{-1} m^2 K ∇^{-1}	Coefficient on non-volcanic forcing anomaly
β_3	W^{-1} m^2 K ∇^{-1}	Coefficient on volcanic forcing anomaly
α	W^{-1} m^2 K ∇^{-1}	Coefficient on incoming radiation less albedo anomaly

variations over time-varying variables such as temperature as in the EBCM of Chavez et al. (2026) that might otherwise require more rigid parametric assumptions. Using the backward difference operator $\triangle$, we discretize the EBCM as

$$\triangle T_{t+1} = \frac{1}{C} Q_t - \frac{1}{C}(A + BT_t) + \frac{1}{C} E_t \tag{3}$$

for years $t = 1, \ldots, T$.

Next, we represent the EBCM in terms of anomalies (changes) relative to an arbitrary base forcing $\bar{E}$, here defined as the 1850-2023 sample average, with forcing anomalies $E_t^* = E_t - \bar{E}$. In this same manner, the anomalies relative to base forcing for temperature and incoming radiation less albedo are $T_t^* = T_t - \bar{T}$ and $Q_t^* = Q_t - \bar{Q}$ where $\bar{T}$ and $\bar{Q}$ are also sample period averages. The

base period equilibrium is subtracted from the EBCM and gives

$$\begin{aligned} \triangle T_{t+1} &= (1/C)Q_t - (1/C)(A + BT_t) + (1/C)E_t \\ -(\triangle \bar{T} &= (1/C)\bar{Q} - (1/C)(A + B\bar{T}) + (1/C)\bar{E}) \\ \hline \triangle T^*_{t+1} &= (1/C)Q^*_t - (B/C)T^*_t + (1/C)E^*_t \end{aligned} \tag{4}$$

where the formula under the horizontal bar is the anomaly representation of the EBCM. In a model such as that of Brock and Miller (2024) in which incoming radiation less albedo is relatively constant, $Q_t = Q = \bar{Q}$ so that $Q^*_t = 0$.

The temperature and forcing data are available from 1850-2024 and 1750-2023, respectively, so our data sample extends from 1850-2023 with 2024 temperature data used to calculate $\triangle T^*_{t+1}$ for 2024. Rewriting the EBCM in anomaly form allows us to simplify estimation by removing the parameter A.

4.2 State-Space Model

To estimate the unobserved variable Q^*_t in equation (4) we use a state-space model (an SSM). An SSM consists of a Markovian state equation that tracks the temporal dynamics of a latent variable and a measurement equation that relates an observed outcome variable (called the observation or measurement variable) to the state variable and other observed covariates (Durbin and Koopman, 2012). A workhorse for structural time series modelers, SSMs have become increasingly utilized in the climate modeling literature (by Bennedsen et al. (2025), for example). In the present context of a zero-dimensional EBCM with time-varying albedo, temperature, forcing, and incoming radiation are observable, but incoming radiation less albedo at the surface is difficult to measure, and we consider it to be latent prior to the satellite era.

We may represent the EBCM in equation (4) in state-space form as

$$y_{t+1} = x_t'\beta + \alpha w_t + u_{t+1} \tag{5}$$

$$w_t = w_{t-1} + v_t \tag{6}$$

$$w_t = w_{t+1} + \eta_t \tag{7}$$

$$\begin{bmatrix} u_{t+1} \\ v_t \end{bmatrix} \sim \textbf{iid}\,\mathbf{N}\left(\begin{bmatrix} 0 \\ 0 \end{bmatrix}, \begin{bmatrix} R & 0 \\ 0 & H \end{bmatrix} \right)$$

with abbreviated notation $y_{t+1} = \triangle T^*_{t+1}$, $x_t = (1, T^*_t, E^{*A}_t, E^{*V}_t)'$, and $w_t = Q^*_t$ for time index $t = 1, \ldots, T-1$, and with $\alpha = 1/C$. Equation (5) is the measurement equation and both equations (6) and (7) are state equations. The former is the standard state equation used to derive and implement the standard Kalman filter (KF), while the latter is a forward-looking "reverse" state

equation used to derive and implement the RKF that we utilize to estimate the partially latent state.

The measurement variable is the change in the temperature anomaly over the next year, while the vector of observed covariates x_t includes this year's forcings and temperature anomalies. Forcing E_t^* has been separated into E_t^{*A} and E_t^{*V} where E_t^{*A} contains all forcing anomalies except for volcanic, solar, land use and BC on snow and E_t^{*V} denotes volcanic forcing anomalies. We omit forcings from solar, land use, and black carbon on snow because these are included in the state variable, the incoming radiation net albedo anomaly (Q_t^*), when it is measured by satellite starting in 2001.

We may expect $\beta = (0, -B/C, 1/C, 1/C)'$ to hold in theory, but we estimate β without restriction. A non-zero intercept β_0 allows series to have means estimated over different time periods, which matters both because T_{t+1}^* and T_t^* have different sample periods and because Q_t^* is observable over a subsample (2001-2023) and therefore cannot be demeaned over the entire sample period (1850-2023). We require $-1 < \beta_1 < 0$ to maintain a stable system, and we find this to be the case without actually imposing the restriction.

Unlike other forcings in the data, effects of volcanic eruptions are very large but dissipate quickly, resulting in the possibility of error in the measurement of the magnitude and timing of volcanic forcing. Although not theoretically justified, the separation of β_2 and β_3 for non-volcanic and volcanic forcings has empirical support due to possible attenuation bias. Specifically, when we include volcanic forcing with the other forcings (results not shown), the coefficient on total forcing is much closer to zero. Previous studies have omitted volcanic forcing (Brock and Miller, 2024) or separated it from other forcings (Kaufmann and Pretis, 2023) as we do.

The series (y_{t+1}) and (x_t) are fully observable, while the series (w_t) is latent through $t = S - 1 = 151$ corresponding to the year 2000, after which point it becomes observable for 23 years until $t = T = 174$. CERES annual net shortwave radiation anomalies at the surface from 2001-2023 render the state variable partially latent. The KF is known to work well with missing data in the measurement variable (Durbin and Koopman, 2012; Li, 2013; Su et al., 2015), in which case the measurement variable can be considered partially latent. However, to the best of our knowledge a partially latent state is rarely considered in the SSM literature, with our search revealing no studies that modify the KF to work with a partially latent state, which seems to be an empirically common occurrence. The RKF provides a logical methodology to address this gap.

We assume the heat capacity of the planet C is constant across time, which is a typical assumption in the integrated assessment model literature. Specifically, both the FUND and PAGE models have constant heat capacity parameters, while DICE has a time-varying heat capacity (Calel and Stainforth, 2017). If instead C varies over time due to variations in ocean heat uptake capacity along the lines of Kosaka and Xie (2013) for example, then the term $-(C_t/C)\Delta T_{t+1}^*$ would appear

in our residuals. It would be difficult to identify time-varying C_t distinctly from time-varying Q_t^*, so we leave this extension for future research.

We may derive the variance of v_t of the state in equation (6) by assuming that the variance of $\triangle w_t$ is H starting from a known initial condition w_0 with no variance. The variance of w_t is therefore given by Ht so that

$$\begin{aligned}\mathbf{var}(v_t) &= \mathbf{var}(w_t - w_{t-1}) = \mathbf{var}(w_t) + \mathbf{var}(w_{t-1}) - 2\mathbf{cov}(w_t, w_{t-1}) \\ &= Ht + H(t-1) - 2H(t-1) = H\end{aligned}$$

as given in the state-space specification.

The reason for showing this derivation is that a similar logic allows us to derive the variance of η_t in the reverse state in equation (7). Rather than starting from known w_0, we start from known w_S and work backwards, so that the variance of w_t is given by $H(S-t)$. Hence

$$\begin{aligned}\mathbf{var}(\eta_t) &= \mathbf{var}(w_t - w_{t+1}) = \mathbf{var}(w_t) + \mathbf{var}(w_{t+1}) - 2\mathbf{cov}(w_t, w_{t+1}) \\ &= H(S-t) + H(S-t-1) - 2H(S-t-1) = H\end{aligned}$$

so that the conditional variances of the two state equations are equal. The equality of these variances results in part from the unit autoregressive parameter of the states. Indeed, if the standard state did not have a unit autoregressive parameter, the reverse state would not have a unit autoregressive parameter, nor would the conditional variances be equal as may be verified using formulas of Taplin (1998).

4.3 Kalman and Reverse Kalman Filters

While the KF starts from a known or estimated point w_0 and works forward, the RKF starts from known w_S and works backward, transitioning from time $t+1$ to time t instead of time $t-1$ to time t. We employ an RKF inspired by that of Taplin (1998) with the key differences being that the previous study considers a measurement equation with the same time indices on either side of the equality and no covariates (x_t).

The KF applied to our state-space model starts at the beginning of the sample, iteratively predicting w_t given $(y_1, \ldots, y_t)$ and then updating that prediction with information contained in y_{t+1}. Instead, the RKF starts at the first observed element w_S of the series (w_t) and works backwards by predicting w_t given $(y_{t+2}, \ldots, y_T)$ and then updating that prediction with information contained in y_{t+1}. We use $\mathcal{F}_t$ to denote the information set driven by present and past values of (y_t) and (x_t), and we use $\mathcal{F}_t^+$ to denote the information set driven by the present and *future* values of (y_t) and (x_{t-2}). The reason for $t-2$ will become clear when we introduce the updating step of

the RKF. We employ the following notations:

$$\begin{aligned} w_{t|s} &= E[w_t|\mathcal{F}_s,] \\ w_{t*s} &= E[w_t|\mathcal{F}_s^+] \\ \omega_{t|s} &= E[(w_t - w_{t|s})^2|\mathcal{F}_s] \\ \omega_{t*s} &= E[(w_t - w_{t*s})^2|\mathcal{F}_s^+] \end{aligned}$$

for general time indices $t, s = 1, \ldots, T$.

The prediction equations of the KF and RKF are given by

$$w_{t|t} = w_{t-1|t} \tag{8}$$

$$w_{t*t+2} = w_{t+1*t+2} \tag{9}$$

respectively, and the updating equations are given by

$$w_{t|t+1} = w_{t|t} + \frac{\alpha\omega_{t|t}}{\alpha^2\omega_{t|t} + R}((y_{t+1} - x_t'\beta) - \alpha w_{t|t}) \tag{10}$$

$$w_{t*t+1} = w_{t*t+2} + \frac{\alpha\omega_{t*t+2}}{\alpha^2\omega_{t*t+2} + R}((y_{t+1} - x_t'\beta) - \alpha w_{t*t+2}) \tag{11}$$

respectively. Note that updating uses new information available from y_{t+1}. For the KF, the new information at time $t+1$ is net of that at time t and earlier from both (y_t) and the observed covariates (x_t), so that the subscripts $t|t$ and $t|t+1$ replace $t|t-1$ and $t|t$ respectively from the familiar case in which the time indices are equal on both side of the measurement equation. For the RKF, the new information at time $t+1$ is net of that at time $t+2$ and later from (y_t), but the information set $\mathcal{F}_t^+$ is defined above so that the information is still net of that from the covariates (x_t) at time t.

As with the KF, the derivation of the updating equation of the RKF relies on normality of the error terms, but normality is unnecessary for estimation. Specifically, the fact that

$$\mathbf{cov}(y_{t+1} - x_t'\beta, w_t - \frac{\alpha\omega_{t*t+2}}{\alpha^2\omega_{t*t+2} + R}((y_{t+1} - x_t'\beta) - \alpha w_{t*t+2})|\mathcal{F}_{t+2}^+) = 0 \tag{12}$$

allows the derivation of the updating equation in equation (11) along the lines of that in the KF, because the first term (in parentheses) of

$$w_t = \left(w_t - \frac{\alpha\omega_{t*t+2}}{\alpha^2\omega_{t*t+2} + R}((y_{t+1} - x_t'\beta) - \alpha w_{t*t+2})\right) + \frac{\alpha\omega_{t*t+2}}{\alpha^2\omega_{t*t+2} + R}((y_{t+1} - x_t'\beta) - \alpha w_{t*t+2}) \tag{13}$$

is conditionally uncorrelated and therefore (by normality) independent of the information conveyed by y_{t+1} conditonally on $\mathcal{F}_t^+$.

The prediction equations of the conditional variance of the state for the KF and RKF are given by

$$\omega_{t|t} = \omega_{t-1|t} + H \tag{14}$$

$$\omega_{t*t+2} = \omega_{t+1*t+2} + H \tag{15}$$

respectively, and the corresponding updating equations are given by

$$\omega_{t|t+1} = \omega_{t|t} + \frac{\alpha^2 \omega_{t|t}^2}{\alpha^2 \omega_{t|t} + R} \tag{16}$$

$$\omega_{t*t+1} = \omega_{t*t+2} + \frac{\alpha^2 \omega_{t*t+2}^2}{\alpha^2 \omega_{t*t+2} + R} \tag{17}$$

respectively. Combining equations (15) and (17) yields

$$\omega_{t-1*t+1} = \omega_{t*t+2} + \frac{\alpha^2 \omega_{t*t+2}^2}{\alpha^2 \omega_{t*t+2} + R} + H,$$

which yields a steady state value of

$$\omega = \frac{H}{2}\left(1 + \sqrt{1 + \frac{4R}{H\alpha^2}}\right) \tag{18}$$

for the series (ω_{t*t+2}) for $t \leqslant S$. It is straightforward to verify that the series $(\omega_{t|t})$ has the same steady state value.

Putting together equations (8) and (10) with the steady state variance ω from equation (18) yields a difference equation in the predicted series $(w_{t|t})$ given by

$$w_{t|t} = \left(\frac{R}{\alpha^2 \omega + R}\right) w_{t-1|t-1} + \frac{\alpha\omega}{\alpha^2 \omega + R}(y_t - x_{t-1}'\beta) \tag{19}$$

for $1 < t \leqslant S$ initiated by an observed value of $w_{1|1} = w_{0|1} = w_0$. Inverting the autoregressive component allows

$$w_{t|t} = \left(\frac{R}{\alpha^2 \omega + R}\right)^{t-1} w_0 + \frac{\alpha\omega}{\alpha^2 \omega + R} \sum_{s=0}^{t-2} \left(\frac{R}{\alpha^2 \omega + R}\right)^s (y_{t-s} - x_{t-1-s}'\beta), \tag{20}$$

which may be used to calculate the likelihood function given below.

Somewhat analogously, combining equations (9) and (11) yields a difference equation in the *updated* series (w_{t*t+1}) given by

$$w_{t*t+1} = \left(\frac{R}{\alpha^2\omega + R}\right) w_{t+1*t+2} + \frac{\alpha\omega}{\alpha^2\omega + R}(y_{t+1} - x_t'\beta) \tag{21}$$

initiated by the observed value of $w_{S*S+1} = w_S$. Inverting the autoregressive component of equation (21) allows

$$w_{t*t+1} = \left(\frac{R}{\alpha^2\omega + R}\right)^{S-t} w_S + \frac{\alpha\omega}{\alpha^2\omega + R} \sum_{s=0}^{S-(t+1)} \left(\frac{R}{\alpha^2\omega + R}\right)^s (y_{t+1+s} - x_{t+s}'\beta) \tag{22}$$

for $t < S$.

Because $|R/(\alpha^2\omega + R)| < 1$, both the KF and RKF in equations (20) and (22) have absolutely summable coefficients even though the state equations in (6) and (7) have unit roots. As a result, the series $(w_{t|t})$ and (w_{t*t+1}) inherit the persistence of $(y_{t+1} - x_t'\beta)$ which need not have a unit root. The series $(y_{t+1} - x_t'\beta)$ preserves the long-run relationship between temperature and forcings that is consistent with physical mechanisms embodied by the EBCM (Kaufmann et al., 2013; Pretis, 2020; Brock and Miller, 2024) without taking a stand on whether the underlying series have unit roots along the lines of Kaufmann et al. (2013) or broken linear trends along the lines of Estrada and Perron (2014), for example.

4.4 Maximum Likelihood Estimation

Taplin (1998) derives an expression for the likelihood of each observation y_t conditioning on past, present, and future information at each point in time. Although the expression treats the forward and backward information sets (nearly) symmetrically, the expression becomes overly complicated in the underlying parameters and would be become more so with different time indices as we have on each side of our measurement equation.

Instead, the joint log likelihood the series (y_t) may be written in the usual way by iteratively conditioning on past information. Using the convention that that $\ell(y_1; \theta) = 0$, we may write the joint log-likelihood as

$$\mathcal{L}(y_1, y_2, \ldots, y_T | x_1, \ldots, x_{T-1}; \theta) = \sum_{t=1}^{T-1} \ell(y_{t+1} | \mathcal{F}_t; \theta) \tag{23}$$

Parameter	Estimate	Significance
β_0	0.1163 (0.0987)	
β_1	−0.6897 (0.0895)	***
β_2	0.2412 (0.0553)	***
β_3	0.0766 (0.0264)	***
$\sqrt{R}$	0.0922 (0.0055)	***
$\sqrt{H}$	0.1319 (0.0829)	
α	0.1004 (0.0651)	
w_0	−1.4365 (1.0870)	

Table 2: Parameter estimates from maximum likelihood estimation of the state space model in equations (5) and (6) estimated using the KF in equation (20) and log-likehood in equations (23) and (24). Standard errors are in parentheses. Statistical significance noted by $^*p < 0.05$, $^{**}p < 0.01$, $^{***}p < 0.001$.

with

$$\ell(y_{t+1}|\mathcal{F}_t,;\theta) = -\frac{1}{2}\ln(\alpha^2\omega + R) - \frac{1}{2(\alpha^2\omega + R)}((y_{t+1} - x_t'\beta) - \alpha w_{t|t})^2 \tag{24}$$

such that $\theta = (\alpha, \beta', R, H)'$ and such that $\omega = 0$ and $w_{t|t} = w_t$ for $t = S+1, \ldots, T-1$. Specifically, after time S, the conditional mean $w_{t|t}$ becomes observable as w_t and its variance $\omega_{t|t}$ immediately drops from its steady state value of ω to zero.

We estimate time-varying albedo as follows. We first run the KF to obtain $w_{t|t}$ and ω. We then estimate the model parameters w_0 and θ using maximum likelihood estimation with the joint log-likelihood in equations (23) and (24). Finally, we run the RKF in equation (21) or (22) using these estimates of θ but discarding w_0.

5 Results and Discussion

The underlying parameter estimates for the partially latent SSM using the KF are shown in Table 2. We estimate $\beta_1 < 0$, which is consistent with a stable system. Moreover, we estimate $(\beta_2, \beta_3) > 0$ as predicted by the facts that both B and C are greater than zero (Brock and Miller, 2024). Note that $\hat{\beta}_3 < \hat{\beta}_2$ (attenuation of $\hat{\beta}_3$ towards zero) is consistent with our expectation based on that fact that that volcanic forcing has is measured with more error than non-volcanic forcing. However, the statistical significance of β_3 at the 1% level shows predictive power of volcanic forcing for temperature changes, which justifies its inclusion in the model.

The main results of the paper are shown in Figure 5. The figure illustrates CERES net shortwave radiation (flux) data from 2001-2023 with net shortwave radiation estimates back to 1850 using

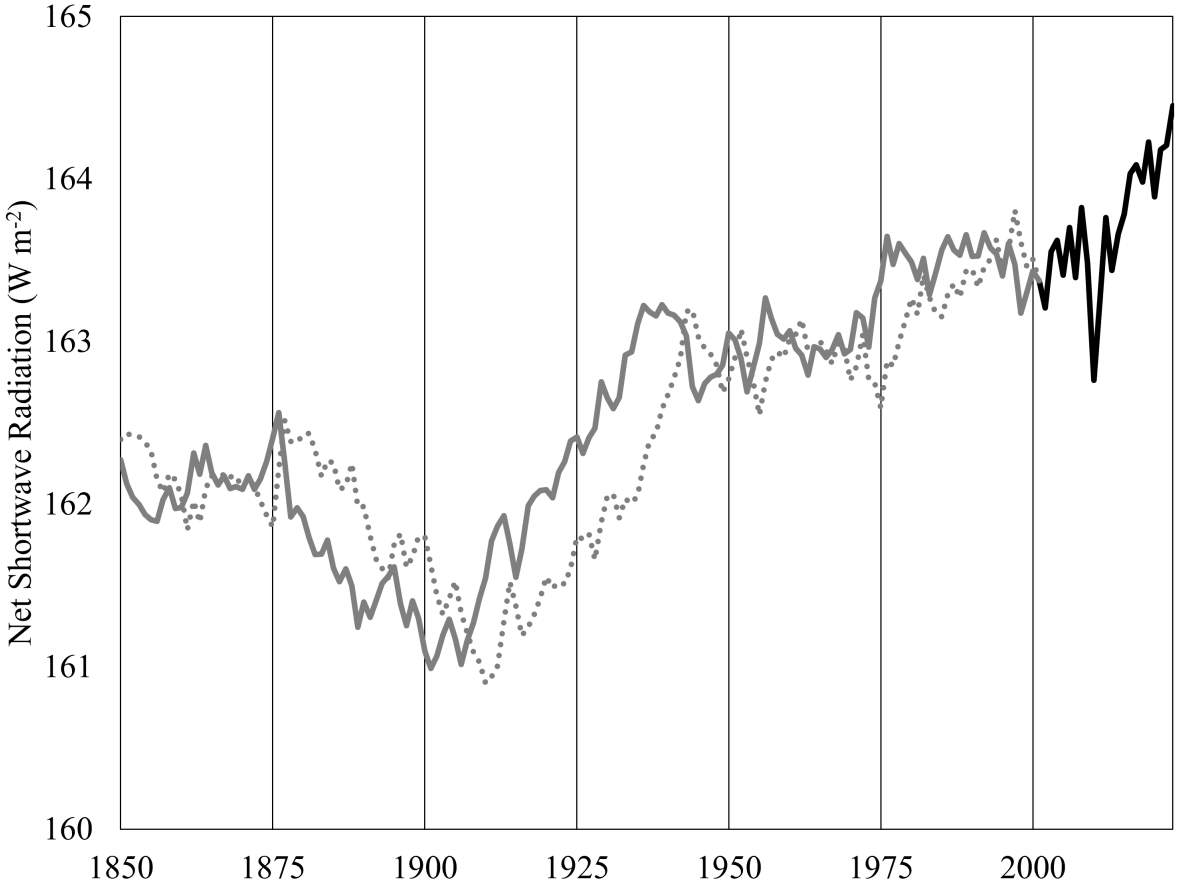


Figure 5: Estimates of net shortwave radiation at the surface from the KF in equation (20) (gray dotted line) and the RKF in equation (22) (gray solid line) prior to 2001. Estimates in 2001 forward (black solid line) are data from CERES collected via satellite and climate calibration.

the RKF. Net shortwave radiation is estimated using the RKF to decrease significantly from 1880 until the first decade of the 20th Century, to a low point of about 161 W m^{-2} in 1900-01 and then again in 1906, and then to increase rapidly until the 1940s. This general pattern is consistent using either filter. However, the dip is estimated with a 5-6 year delay using the KF relative to the RKF.

Our primary interpretation uses post-1940 estimates where we have more reliable temperature data. Post-1940 fluxes estimated using both the KF and RKF show a roughly increasing trend that corresponds to decreasing reflection from the surface assuming roughly constant incoming solar radiation. Both the KF and RKF estimate approximately the same flux in 1943, and the total increase over 1943-2023 is estimated to be approximately 1.5 W m^{-2}. The minimum net shortwave radiation in the post-1940 sample is estimated to be 162.6 W m^{-2} in 1945 (with a major dip in 2010 to 162.7 W m^{-2}) and the maximum is estimated to be 164.4 W m^{-2} in 2023.

5.1 Anthropogenic and Natural Effects on Albedo

It is widely accepted that CO_2 emissions increase surface temperatures through the greenhouse effect (Mitchell, 1989), and indeed this is one of the premises of the EBCM model. The forcing data that we utilize show an effect of CO_2 emissions over 1943-2023 of 1.6 W m^{-2}. Notably, the increase of 1.5 W m^{-2} in surface albedo that we detect over the same period is almost as large. Sea ice is a large contributor to albedo, and the generally declining albedo pattern that we find is consistent with the projections on arctic sea ice shrinkage of Diebold and Rudebusch (2022, 2023). The earlier study finds that shrinkage is accelerating and forecast an ice-free Arctic September appearing sometime in the 2030s with 60% probability.

The increasing-decreasing reflection trends in our estimates could potentially be explained by endogenous temperature cycles – i.e., natural climate variability. For example, Kosaka and Xie (2013) provide evidence that the 1998-2013 global warming hiatus may have been caused by cooling in the eastern equatorial Pacific Ocean. Specifically, they conduct experiments with a Global Climate Model where radiative forcings and eastern equatorial Pacific sea surface temperatures (SSTs) are observed and allow all other global surface temperatures to be simulated. When restricting the Pacific SSTs, the model closely simulates the global warming hiatus and other important regional climate events. Given that climate models predict Pacific warming in response to the observed 1998-2013 increase in forcings, the authors suggest the Pacific cooling is due to a natural cycle.

Given the significance of Pacific cooling on global surface temperatures, it is plausible that natural ocean heat cycles influence albedo through ice formation. While Kosaka and Xie (2013) do not explicitly mention changes in albedo as an effect of the Pacific cooling, the 1998-2013 hiatus corresponds to a period of relatively low net shortwave radiation in Figure 5. Specifically, 1998 shows a local minimum of 163.2 W m^{-2} after a period since the 1970s when it mostly exceeds 163.4 W m^{-2}. While net shortwave radiation increased again after 1998, it hit another low of 162.8 W m^{-2} in 2010. Interestingly, Kosaka and Xie (2013) also show a decrease in September Arctic sea ice extent over the hiatus period, suggesting that Pacific cooling may have prevented further sea ice loss than was observed over this period.

Miller and Nam (2020) also study a long-term ocean heat cycle as an explanation of the 1998-2013 global warming hiatus. The authors estimate a long-term cycle they refer to as the Oceanic Multidecadal Oscillation (OMO), related the the more well-known Atlantic Multidecadal Oscillation, which shows a peak in $\sim$2023, the minimum of reflectiveness in our estimates. Similarly, Miller and Nam (2020) estimate a trough of the OMO in $\sim$1978 which precedes a period of decreasing reflection in Figure 5. Therefore, it appears plausible that a long-term ocean heat cycle is a contributing factor to surface albedo.

The El Nino Southern Oscillation (ENSO) is a higher frequency coupled ocean-atmosphere feedback which causes regional climate variability and whose warm and cool periods are termed

El Niño and La Niña respectively. According to Timmermann et al. (2018) the Nino3 SSTA index that is used to determine El Niño events peaked in ∼1983, 1988, 1998 and 2016. However, these dates do not correspond to positive peaks in net shortwave radiation in our figure, so we cannot conclude that ENSO has a noticeable effect on albedo based on our results.

Wyatt and Curry (2014) point out that many previously studied climate fluctuations coordinate with over approximately ∼50-80 year cycles, a phenomenon they refer to as the stadium wave. Previous studies found a cycle running around the Northern Hemisphere by longitude, hence the stadium wave analogy where fans in an arena stand up by section. They explore physical mechanisms that could explain the pattern, and find that the Eurasian Arctic sea ice shelf forming and un-forming may explain much of the stadium wave pattern.

Given the significance of sea ice in the SAF, it is plausible that cool periods defined by large amounts of sea ice would correspond to increased albedo and hot periods with reduced sea ice would similarly correspond to decreased albedo. Wyatt and Curry (2014) specifically identify 1976-1998 as a warming regime of the stadium wave cycle and 1944-1971 as a cooling regime of the cycle. Looking at Figure 5, our estimates show roughly decreased and increased reflectiveness during these respective time periods, suggesting that the stadium wave pattern correlates with surface albedo.

5.2 Implications for Carbon Pricing

How does the SAF affect carbon pricing? The IAM literature utilizes future temperature scenarios to estimate economic damages resulting from climate change (Calel and Stainforth, 2017) which lead to estimates of the cost of emitting carbon – i.e., carbon prices. IAMs rely on climate sensitivity, often embodied by the so-called transient climate response or equilibrium climate sensitivity. These measure the Earth's temperature response to a doubling of CO_2 concentration in the atmosphere, but differ by the time scale on which they operate. If an IAM underestimates climate sensitivity and hence how fast temperature will change in response to forcing, it will underestimate the negative consequences of emitting more carbon and hence carbon will be underpriced.

Well-known IAMs FUND and PAGE are based on a zero-dimensional EBCM with a time-invariant incoming radiation less albedo term of the form

$$\partial_t T^*(t) = -\frac{B}{C} T^*(t) + \frac{1}{C} E^*(t) \tag{25}$$

with notation defined as above (Calel and Stainforth, 2017). An Euler approximation of the EBCM may be written as

$$\Delta T^*_{t+1} = -\frac{B}{C} T^*_t + \frac{1}{C} E^*_t, \tag{26}$$

Parameter	Estimate	Significance
β_0	0.0055 (0.0078)	
β_1	−0.4418 (0.0637)	***
β_2	0.2136 (0.0306)	***
β_3	0.0484 (0.0264)	*

Table 3: Parameter estimates from least squares estimation of the simple EBCM/IAM in equation (27). Standard errors are in parentheses. Statistical significance noted by $^*p < 0.05$, $^{**}p < 0.01$, $^{***}p < 0.001$.

for $t = 1, \ldots, T$, and we may estimate the EBCM using

$$y_{t+1} = x_t'\beta + \varepsilon_{t+1}, \tag{27}$$

using the notation introduced for the state-space model above.

Compared to that in equation (2) estimated by the system in equations (5)-(7), the EBCM in equation (25) estimated by the regression in (27) approximates temperature change as a linear function of past forcings and temperature, omitting any variation in albedo over time. However, if albedo changes as a nonlinear declining function of temperature, as predicted by SAF theory, a declining albedo term will appear in the EBCM residuals. Because forcing increases temperature, additional forcing will also decrease albedo thereby leading to an acceleration of climate change and hence faster heating than predicted by the linear model.

Suppose that albedo is explicitly modeled as a decreasing function of temperature, leading to a model of the form

$$\Delta T^*_{t+1} = \frac{1}{C}E^*_t - \frac{B}{C}T^*_t + \frac{Q}{C}(1 - a(T^*_t)) \tag{28}$$

where Q is constant incoming solar radiation to the surface and $a(T^*_t)$ is albedo. Estimating the regression in equation (27) without including time-varying albedo in equation (28) would result in the term $(Q/C)(1 - a(T^*_t))$ appearing as an increasing trend in the residuals as temperatures rise. And if an IAM sets a carbon price as a function of a predicted temperature path in response to forcing, omitting $a(T^*_t)$ leads to a slower predicted increase in temperatures thereby resulting in underestimation of the cost of carbon emissions.

Our results in Figure 5 show an increasing trend in net shortwave radiation, consistent with the finding of decreasing arctic ice extent from 1979 to 2019 (Diebold and Rudebusch, 2023) which would contribute to decreasing albedo through the SAF (Kaufmann and Pretis, 2023). In contrast, there is no obvious trend in the residuals of the regression in equation (27), as shown in Figure 6.

Why might that be? Suppose that $a(T^*_t) = -aT^*_t$ for $a > 0$ – i.e., that albedo is a decreasing linear function of temperature. The temperature coefficient of the EBCM will absorb the effects of

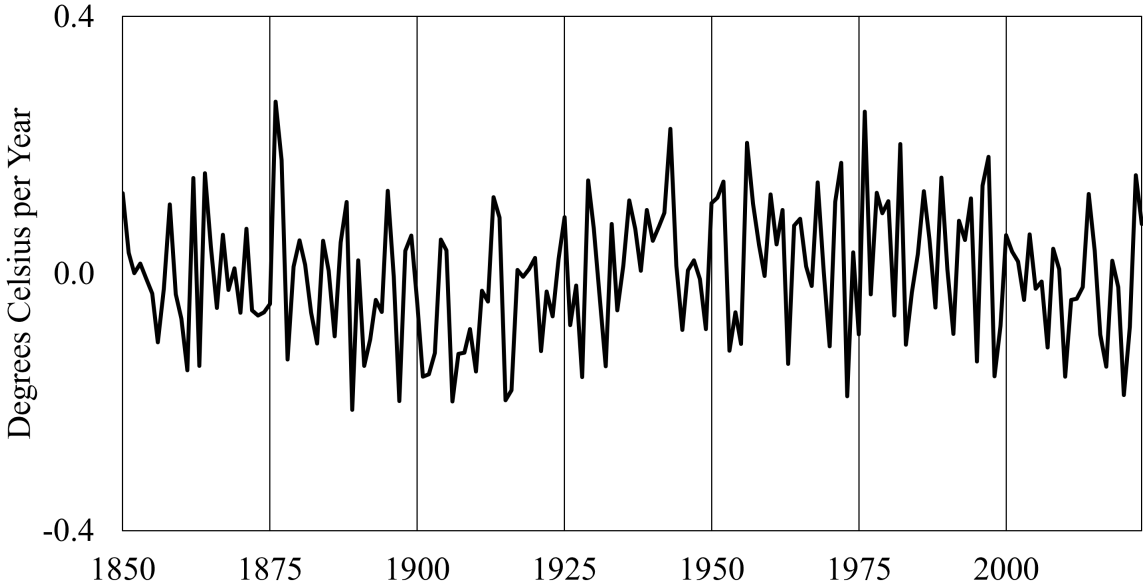


Figure 6: Residuals from least squares estimation of the simple EBCM/IAM in equation (27).

albedo decline and attenuate to zero, becoming $-(B-aQ)/C$. The linear specification of the EBCM is similarly prone to underpricing if the SAF mechanism is a more general decreasing function of temperature. Indeed, the results of estimating the regression in equation (27), shown in Table 3, support the attenuation bias. Compared to our estimates in Table 2, we note an estimate of β_1 closer to zero (-0.44 vs. -0.69), which suggests that the temperature coefficient is absorbing the albedo decline and somewhat accounting for the SAF. Specifically, $-(B/C)T_t^* + (Q/C)(1 - a(T_t^*))$ is the temperature-related component of the IAM in equation (28), and the attenuation of the estimate of β_1 suggests that the $(Q/C)(1 - a(T_t^*))$ is not constant.

6 Conclusion

A goal of climate economics is to understand the delicate balance between economic activity and climate degradation. To this end, IAMs have been developed to measure the costs of carbon emissions and limit economic activity only to the extent that the climate benefits exceed costs of reduced production (Weyant, 2017). Given recent broad implementation of carbon taxes and tradable pollution permits (Coria and Sterner, 2010; Narassimhan et al., 2018) it is necessary to consider whether the policies put in place are fully measuring effects of carbon emissions on global temperatures. Along these lines, Diebold and Rudebusch (2023) show that large-scale climate models in CMIP5 and CMIP6 underestimate the rate at which we will arrive at an ice-free arctic if carbon emissions continue at current rates, which highlights both a need for research on Arctic

climate feedbacks and the potential of even highly complex climate models to underestimate effects from nonlinear feedbacks.

Leveraging satellite data and historical data on temperature anomalies and forcings, we develop and employ an RKF procedure with an SSM representation of a zero-dimensional EBCM to estimate annual global surface albedo over a longer time span, 1850-2023, than previous studies that have been limited to periods where satellite data is available (Henderson-Sellers and Wilson, 1983; Stephens et al., 2015; Mengyao et al., 2023).

We find albedo to be decreasing since at least the 1940s when the temperature anomaly data become more reliable. Controlling for trends in temperature and carbon emissions, an additional trend in albedo suggests that the warming effect of carbon emissions is amplified by the SAF and that assuming constant albedo has the potential to underprice carbon emissions by omitting a time-varying albedo term. Underpricing may occur due to a decreasing function of temperature – i.e., surface albedo – causing underestimation of the speed of temperature increases. Therefore, our research highlights the need for continued tracking of albedo over time and the addition of the SAF to contemporary carbon pricing models.

References

Abbott, C. and F. Fowle (1908). Recent determination of the solar constant of radiation. *Terrestrial Magnetism and Atmospheric Electricity 13*, 79–82.

Alajingi, R. and R. Marimuthu (2023). Novel classification of energy sources, with implications for carbon emissions. *Energy Strategy Reviews 49*, 101146.

Baranzini, A., J. C. Van den Bergh, S. Carattini, R. B. Howarth, E. Padilla, and J. Roca (2017). Carbon pricing in climate policy: Seven reasons, complementary instruments, and political economy considerations. *Wiley Interdisciplinary Reviews: Climate Change 8*, e462.

Bennedsen, M., E. Hillebrand, and S. J. Koopman (2025). A Statistical Reduced Complexity Climate Model for Probabilistic Analyses and Projections. *Journal of Climate 38*, 6329–6350.

Bond, G. P. (1861). On the light of the Moon and of the Planet Jupiter. *Memoirs of the American Academy of Arts and Sciences 8*, 221–286.

Brock, W. A. and J. I. Miller (2024). Polar amplification in a moist energy balance model: A structural econometric approach to estimation and testing. *Journal of Econometrics 245*, 105885.

Budyko, M. I. (1969). The effect of solar radiation variations on the climate of the Earth. *tellus 21*, 611–619.

Calel, R. and D. A. Stainforth (2017). On the physics of three integrated assessment models. *Bulletin of the American Meteorological Society 98*, 1199–1216.

Castle, J. L., D. F. Hendry, and J. I. Miller (2024). Econometric Forecasting of Climate Change. In M. Clements and A. Galv ao (Eds.), *Handbook of Research Methods and Applications in Macroeconomic Forecasting*. Cheltenham, UK: Edward Elgar Publishing. https://doi.org/10.4337/9781035310050.00018.

Chavez, E., J. Rombouts, and M. Ghil (2026). A stable hothouse triggered by a tipping mechanism Open Access. *Philosophical Transactions of the Royal Society A 384*, 20240489.

Coria, J. and T. Sterner (2010). Tradable permits in developing countries: Evidence from air pollution in Chile. *The Journal of Environment & Development 19*, 145–170.

Cotana, F., F. Rossi, M. Filipponi, V. Coccia, A. L. Pisello, E. Bonamente, A. Petrozzi, and G. Cavalaglio (2014). Albedo control as an effective strategy to tackle Global Warming: A case study. *Applied Energy 130*, 641–647.

Danjon, A. (1928). Recherches de photométrie astronomique. *Annales de l'Observatoire de Strasbourg, vol. 2, pp. 1-185 2*, 1–185.

Danjon, A. (1933). Nouvelles Recherches Sur la Photométrie de la Lumière Cendrée et l'Albedo de la Terre. *Annales de l'Observatoire de Strasbourg, vol. 3, pp. 138.1-179.2 3*, 138.1–179.2.

Diebold, F. X. and G. D. Rudebusch (2022). Probability assessments of an ice-free Arctic: Comparing statistical and climate model projections. *Journal of Econometrics 231*, 520–534.

Diebold, F. X. and G. D. Rudebusch (2023). Climate models underestimate the sensitivity of Arctic sea ice to carbon emissions. *Energy Economics 126*, 107012.

Durbin, J. and S. J. Koopman (2012). *Time series analysis by state space methods* (2nd ed.). Oxford, UK: OUP Oxford.

Déry, S. J. and R. D. Brown (2007). Recent Northern Hemisphere snow cover extent trends and implications for the snow-albedo feedback. *Geophysical Research Letters 34*.

Estrada, F. and P. Perron (2014). Detection and attribution of climate change through econometric methods. *Boletín de la Sociedad Matemática Mexicana 20*, 107–136.

Folland, C. K. and D. Parker (1995). Correction of instrumental biases in historical sea surface temperature data. *Quarterly Journal of the Royal Meteorological Society 121*, 319–367.

Forster, P., T. Storelvmo, K. Armour, W. Collins, J.-L. Dufresne, D. Frame, D. Lunt, T. Mauritsen, M. Palmer, M. Watanabe, M. Wild, and H. Zhang (2021). The Earth's Energy Budget, Climate Feedbacks, and Climate Sensitivity. In *Climate Change 2021: The Physical Science Basis. Contribution of Working Group I to the Sixth Assessment Report of the Intergovernmental Panel on Climate Change*, pp. 923–1054. Cambridge, United Kingdom and New York, NY, USA: Cambridge University Press.

Forster, P. M., C. Smith, T. Walsh, W. F. Lamb, R. Lamboll, B. Hall, M. Hauser, A. Ribes, D. Rosen, and N. P. Gillett (2024). Indicators of Global Climate Change 2023: Annual update of key indicators of the state of the climate system and human influence. *Earth System Science Data 16*, 2625–2658.

Fraser, D. C. and J. E. Potter (1969). The Optimun Linear Smoother as a Combination of Two Optimum Linear Filters. *IEEE Transactions on Automatic Control 14*, 387–390.

Fritz, S. (1949). The albedo of the planet Earth and of clouds. *Journal of Atmospheric Sciences 6*, 277–282.

Goode, P. R., E. Pallé, A. Shoumko, S. Shoumko, P. Montañes-Rodriguez, and S. Koonin (2021). Earth's albedo 1998–2017 as measured from earthshine. *Geophysical Research Letters 48*, e2021GL094888.

Goode, P. R., J. Qiu, V. Yurchyshyn, J. Hickey, M. Chu, E. Kolbe, C. Brown, and S. Koonin (2001). Earthshine observations of the Earth's reflectance. *Geophysical Research Letters 28*, 1671–1674.

Hadley, O. L. and T. W. Kirchstetter (2012). Black-carbon reduction of snow albedo. *Nature Climate Change 2*, 437–440.

Hansen, J. E., P. Kharecha, M. Sato, G. Tselioudis, J. Kelly, S. E. Bauer, R. Ruedy, E. Jeong, Q. Jin, and E. Rignot (2025). Global Warming Has Accelerated: Are the United Nations and the Public Well-Informed? *Environment: Science and Policy for Sustainable Development 67*, 6–44.

He, T., S. Liang, and D. Song (2014). Analysis of global land surface albedo climatology and spatial-temporal variation during 1981–2010 from multiple satellite products. *Journal of Geophysical Research: Atmospheres 119*, 10,281–10,298.

Held, I. M. and M. J. Suarez (1974). Simple albedo feedback models of the icecaps. *Tellus 26*, 613–629.

Henderson-Sellers, A. and M. F. Wilson (1983). Surface albedo data for climatic modeling. *Reviews of Geophysics 21*, 1743–1778.

Houghton, H. G. (1954). On the annual heat balance of the Northern Hemisphere. *Journal of Atmospheric Sciences 11*, 1–9.

Hu, Y., G. Jia, C. Pohl, X. Zhang, and J. van Genderen (2016). Assessing surface albedo change and its induced radiation budget under rapid urbanization with Landsat and GLASS data. *Theoretical and Applied Climatology 123*, 711–722.

Huang, Y., P. C. Taylor, F. G. Rose, D. A. Rutan, M. D. Shupe, M. A. Webster, and M. M. Smith (2022). Toward a more realistic representation of surface albedo in NASA CERES-derived surface radiative fluxes: A comparison with the MOSAiC field campaign: Comparison of CERES and MOSAiC surface radiation fluxes. *Elem Sci Anth 10*, 00013.

Hunt, G. E., R. Kandel, and A. T. Mecherikunnel (1986). A history of presatellite investigations of the Earth's radiation budget. *Reviews of geophysics 24*, 351–356.

Jenkins, J. D. (2014). Political economy constraints on carbon pricing policies: What are the implications for economic efficiency, environmental efficacy, and climate policy design? *Energy Policy 69*, 467–477.

Jones, P. D. and A. Moberg (2003). Hemispheric and large-scale surface air temperature variations: An extensive revision and an update to 2001. *Journal of climate 16*, 206–223.

Kang, S., Y. Zhang, Y. Qian, and H. Wang (2020). A review of black carbon in snow and ice and its impact on the cryosphere. *Earth-science reviews 210*, 103346.

Kato, S. (2009). Interannual variability of the global radiation budget. *Journal of climate 22*, 4893–4907.

Kato, S., N. G. Loeb, F. G. Rose, S.-H. Ham, T. J. Thorsen, D. A. Rutan, W. F. Miller, T. E. Caldwell, D. R. Doelling, and S. Sun-Mack (2025). Seamless continuity in CERES Energy Balanced and Filled (EBAF) surface radiation budget across multiple satellites. *Journal of Climate 38*, 2461–2478.

Kato, S., F. G. Rose, D. A. Rutan, T. J. Thorsen, N. G. Loeb, D. R. Doelling, X. Huang, W. L. Smith, W. Su, and S.-H. Ham (2018). Surface irradiances of edition 4.0 clouds and the Earth's radiant energy system (CERES) energy balanced and filled (EBAF) data product. *Journal of Climate 31*, 4501–4527.

Kaufmann, R. K., H. Kauppi, M. L. Mann, and J. H. Stock (2013). Does temperature contain a stochastic trend: linking statistical results to physical mechanisms. *Climatic change 118*, 729–743.

Kaufmann, R. K. and F. Pretis (2023). An empirical estimate for the snow albedo feedback effect. *Climatic Change 176*, 107.

Kennedy, J. J., N. Rayner, C. Atkinson, and R. Killick (2019). An ensemble data set of sea surface temperature change from 1850: The Met Office Hadley Centre HadSST. 4.0. 0.0 data set. *Journal of Geophysical Research: Atmospheres 124*, 7719–7763.

Kennedy, J. J., N. A. Rayner, R. O. Smith, D. E. Parker, and M. Saunby (2011). Reassessing biases and other uncertainties in sea surface temperature observations measured in situ since 1850: 2. Biases and homogenization. *Journal of Geophysical Research: Atmospheres 116*.

Knight, J. R., C. K. Folland, and A. A. Scaife (2006). Climate impacts of the Atlantic multidecadal oscillation. *Geophysical Research Letters 33*.

Kosaka, Y. and S.-P. Xie (2013). Recent global-warming hiatus tied to equatorial Pacific surface cooling. *nature 501*, 403–407.

Li, B. (2013). State estimation with partially observed inputs: A unified Kalman filtering approach. *Automatica 49*, 816–820.

Li, Z. and L. Garand (1994). Estimation of surface albedo from space: A parameterization for global application. *Journal of Geophysical Research: Atmospheres 99*, 8335–8350.

Liang, S., D. Wang, T. He, and Y. Yu (2019). Remote sensing of Earth's energy budget: Synthesis and review. *International Journal of Digital Earth 12*, 737–780.

Loeb, N. G., M. Mayer, S. Kato, J. T. Fasullo, H. Zuo, R. Senan, J. M. Lyman, G. C. Johnson, and M. Balmaseda (2022). Evaluating twenty-year trends in Earth's energy flows from observations and reanalyses. *Journal of Geophysical Research: Atmospheres 127*, e2022JD036686.

Mach, E. (2013). *The principles of physical optics: an historical and philosophical treatment* (1st ed.). Mineola, NY: Courier Corporation.

Mengyao, L., L. Qiang, and Q. Ying (2023). A comparative study of long-time series of global-scale albedo products. *International Journal of Digital Earth 16*, 308–322.

Miller, J. I. and K. Nam (2020). Dating hiatuses: A statistical model of the recent slowdown in global warming and the next one. *Earth Syst. Dynam. 11*, 1123–1132.

Mitchell, J. F. (1989). The "greenhouse" effect and climate change. *Reviews of Geophysics 27*, 115–139.

Mylne, M. and P. Rowntree (1992). Modelling the effects of albedo change associated with tropical deforestation. *Climatic Change 21*, 317–343.

Narassimhan, E., K. S. Gallagher, S. Koester, and J. R. Alejo (2018). Carbon pricing in practice: A review of existing emissions trading systems. *Climate Policy 18*, 967–991.

Nikolov, N. and K. F. Zeller (2024). Roles of Earth's Albedo Variations and Top-of-the-Atmosphere Energy Imbalance in Recent Warming: New Insights from Satellite and Surface Observations. *Geomatics 4*, 311–341.

North, G. R. and K.-Y. Kim (2017). *Energy balance climate models* (1st ed.). Hoboken, NJ: John Wiley & Sons.

Ouyang, Z., P. Sciusco, T. Jiao, S. Feron, C. Lei, F. Li, R. John, P. Fan, X. Li, and C. A. Williams (2022). Albedo changes caused by future urbanization contribute to global warming. *Nature communications 13*, 3800.

Perkins, S. (2020). Core Concept: Albedo is a simple concept that plays complicated roles in climate and astronomy (vol 116, pg 25369, 2019). *PROCEEDINGS OF THE NATIONAL ACADEMY OF SCIENCES OF THE UNITED STATES OF AMERICA 117*, 1816–1816.

Pretis, F. (2020). Econometric modelling of climate systems: The equivalence of energy balance models and cointegrated vector autoregressions. *Journal of Econometrics 214*, 256–273.

Previdi, M., K. L. Smith, and L. M. Polvani (2021). Arctic amplification of climate change: a review of underlying mechanisms. *Environmental Research Letters 16*, 093003.

Qu, X. and A. Hall (2007). What controls the strength of snow-albedo feedback? *Journal of Climate 20*, 3971–3981.

Qu, X. and A. Hall (2014). On the persistent spread in snow-albedo feedback. *Climate dynamics 42*, 69–81.

Qu, Y., S. Liang, Q. Liu, T. He, S. Liu, and X. Li (2015). Mapping surface broadband albedo from satellite observations: A review of literatures on algorithms and products. *Remote Sensing 7*, 990–1020.

Riihelä, A., E. Jääskeläinen, and V. Kallio-Myers (2024). Four decades of global surface albedo estimates in the third edition of the CM SAF Cloud, Albedo and surface Radiation (CLARA) climate data record. *Earth System Science Data 16*, 1007–1028.

Santos Orozco, D. L., J. A. Ruiz Corral, R. F. Villavicencio García, and V. M. Rodríguez Moreno (2023). Deforestation and Its Effect on Surface Albedo and Weather Patterns. *Sustainability 15*, 11531.

Sellers, W. D. (1969). A global climatic model based on the energy balance of the Earth-atmosphere system. *Journal of Applied Meteorology 8*, 392–400.

Song, Y., M. Lv, M. Wang, X. Li, and Y. Qu (2021). Reconstruction of historical land surface albedo changes in China from 850 to 2015 using land use harmonization data and albedo look-up maps. *Earth and Space Science 8*, e2021EA001799.

Stephens, G. L., D. O'Brien, P. J. Webster, P. Pilewski, S. Kato, and J. Li (2015). The albedo of Earth. *Reviews of geophysics 53*, 141–163.

Su, J., B. Li, and W.-H. Chen (2015). On existence, optimality and asymptotic stability of the Kalman filter with partially observed inputs. *Automatica 53*, 149–154.

Tang, R., X. Zhao, T. Zhou, B. Jiang, D. Wu, and B. Tang (2018). Assessing the impacts of urbanization on albedo in Jing-Jin-Ji Region of China. *Remote Sensing 10*, 1096.

Taplin, R. H. (1998). The reverse kalman filter. *Communications in Statistics: Theory and Methods 27*, 2547–2558.

Thackeray, C. W. and C. G. Fletcher (2016). Snow albedo feedback: Current knowledge, importance, outstanding issues and future directions. *Progress in Physical Geography 40*, 392–408.

Timmermann, A., S.-I. An, J.-S. Kug, F.-F. Jin, W. Cai, A. Capotondi, K. M. Cobb, M. Lengaigne, M. J. McPhaden, and M. F. Stuecker (2018). El Niño–southern oscillation complexity. *Nature 559*, 535–545.

Trenberth, K. E., J. T. Fasullo, and J. Kiehl (2009). Earth's Global Energy Budget. *Bulletin of the American Meteorological Society 90*, 311–324.

Very, F. W. (1913). The Earth's albedo. *Astronomische Nachrichten 196*, 269.

Weyant, J. (2017). Some Contributions of Integrated Assessment Models of Global Climate Change. *Review of Environmental Economics and Policy 11*, 115–137.

Wild, M., M. Z. Hakuba, D. Folini, P. Dörig-Ott, C. Schär, S. Kato, and C. N. Long (2019). The cloud-free global energy balance and inferred cloud radiative effects: An assessment based on direct observations and climate models. *Climate Dynamics 52*, 4787–4812.

Williamson, C. J., J. Cook, A. Tedstone, M. Yallop, J. McCutcheon, E. Poniecka, D. Campbell, T. Irvine-Fynn, J. McQuaid, and M. Tranter (2020). Algal photophysiology drives darkening and melt of the Greenland Ice Sheet. *Proceedings of the National Academy of Sciences 117*, 5694–5705.

Wu, J., E. Pallé, H. Guo, and Y. Ding (2023). Long-term trends in albedo as seen from a lunar observatory. *Advances in Space Research 72*, 2109–2117.

Wyatt, M. G. and J. A. Curry (2014). Role for Eurasian Arctic shelf sea ice in a secularly varying hemispheric climate signal during the 20th century. *Climate Dynamics 42*, 2763–2782.

Zhan, C., R. P. Allan, S. Liang, D. Wang, and Z. Song (2019). Evaluation of five satellite top-of-atmosphere albedo products over land. *Remote Sensing 11*, 2919.

Zhan, C. and S. Liang (2022). Improved estimation of the global top-of-atmosphere albedo from AVHRR data. *Remote Sensing of Environment 269*, 112836.